

Indoor Multi-View Radar Object Detection via 3D Bounding Box Diffusion

Ryoma Yataka^{1,2*}, Pu (Perry) Wang², Petros Boufounos², Ryuhei Takahashi¹

¹Information Technology R&D Center (ITC), Mitsubishi Electric Corporation (MELCO), Kanagawa 247-8501, Japan

²Mitsubishi Electric Research Laboratories (MERL), Cambridge, MA 02139, USA

Abstract

Multi-view indoor radar perception has drawn attention due to its cost-effectiveness and low privacy risks. Existing methods often rely on implicit cross-view radar feature association, such as proposal pairing in RFMask or query-to-feature cross-attention in RETR, which can lead to ambiguous feature matches and degraded detection in complex indoor scenes. To address these limitations, we propose **REXO** (multi-view Radar object dEction with 3D bounding box diffusiOn), which lifts the 2D bounding box (BBox) diffusion process of DiffusionDet into the 3D radar space. REXO utilizes these noisy 3D BBoxes to guide an explicit cross-view radar feature association, enhancing the cross-view radar-conditioned denoising process. By accounting for prior knowledge that the person is in contact with the ground, REXO reduces the number of diffusion parameters by determining them from this prior. Evaluated on two open indoor radar datasets, our approach surpasses state-of-the-art methods by a margin of +4.22 AP on the HIBER dataset and +11.02 AP on the MMVR dataset.

1 Introduction

Radar perception has received increasing attention due to its robustness in low-light, adversarial weather, and hazardous conditions (e.g., smoke) (Paek et al. 2022; Yao et al. 2024; Lu et al. 2020; Sun, Petropulu, and Poor 2020; Pandharpande et al. 2023; Skog et al. 2024). Depending on the application, operational specifications, and downstream tasks, radar data can be represented in different forms such as sparse detection points (Zhao et al. 2017; Sengupta et al. 2020; Yang et al. 2023b), reflection heatmaps (Adib et al. 2015; Zhao et al. 2018a; Wu et al. 2023), Doppler signatures, and raw analog-to-digital converter (ADC) data, each with unique characteristics and feature granularity.

For indoor radar perception, single-view and multi-view heatmaps that combine horizontal (depth-horizontal) and vertical (depth-vertical) projections enable object detection, pose estimation, and segmentation on a 2D image plane (Zhao et al. 2018a; Lee et al. 2023; Wu et al. 2023; Rahman et al. 2024). RF-Pose (Zhao et al. 2018a,b) first fused both views with a convolutional autoencoder to regress 2D human keypoints. RFMask (Wu et al. 2023) grafted Faster R-CNN (Ren et al. 2017) onto horizontal heatmaps:

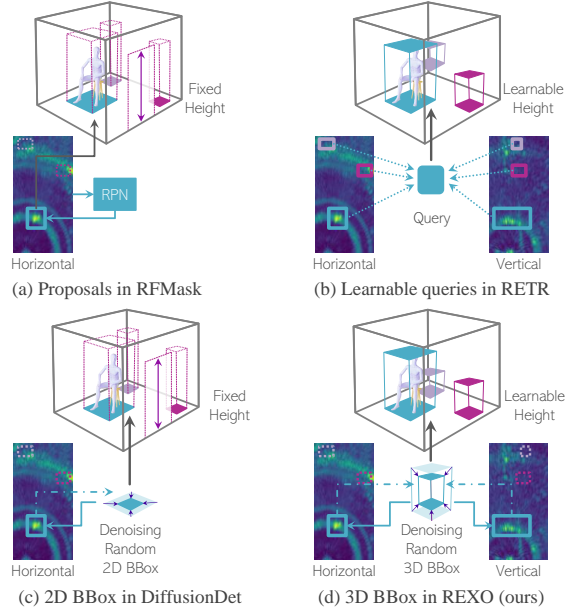


Figure 1: (a) RFMask (Wu et al. 2023) generates horizontal-view proposals with fixed-height vertical boxes; (b) RETR (Yataka et al. 2024) implicitly links queries to cross-view features via decoder cross-attention; (c) DiffusionDet (Chen et al. 2023b) adapted to horizontal radar allows 2D denoising but needs extra pairing with fixed-height vertical boxes; (d) REXO (ours) performs diffusion directly in 3D radar space for simple, explicit cross-view association.

its region-proposal network produces horizontal candidates that are paired with fixed-height vertical windows to avoid exhaustive cross-view association (Fig. 1 (a)). More recently, the radar detection transformer (RETR) (Yataka et al. 2024) adopted the DETR (Carion et al. 2020). Decoder queries simultaneously attend to both views through cross-attention (Fig. 1 (b)) and are directly regressed to 3D bounding boxes (BBoxes) that are classified as person or background.

On the other hand, image-based object detection has been redefined as a generative denoising process, where random noisy 2D BBoxes are iteratively refined through a diffusion denoising process to yield final clean BBox predictions (Chen et al. 2023b). Referred to as DiffusionDet, it decouples training and inference, and generally surpasses

*The work was done as a visiting scientist of MERL from ITC.

query-based detectors. When ported to horizontal radar heatmaps (Fig. 1 (c)), it denoises 2D boxes but still requires the fixed-height vertical pairing used by RFMask.

We therefore *lift* the diffusion procedure from a 2D plane (image or horizontal radar view) in DiffusionDet to the full 3D radar space, as illustrated in Fig. 1 (d). This simple lifting facilitates cross-view radar feature association and radar-conditioned BBox denoising, while enabling the integration of geometry-aware loss functions and prior constraints on the 3D BBox. Consequently, we introduce the proposed framework as **Radar object dEtection with 3D bounding boX diffusiOn (REXO)** with the following contributions:

1. **2D-to-3D Lifting with Explicit Cross-View Association:** At each diffusion timestep, noisy 3D BBoxes are projected onto every radar view, and ROI-aligned crops supply view-specific features. This BBox-guided association grows *linearly* with the number of views, whereas proposal- or query-based schemes grow quadratically.
2. **Cross-View Radar-Conditioned BBox Detection:** While the cross-view feature association is simplified due to the 2D-to-3D lifting, the denoising process may be more challenging. In turn, the associated radar features are used as conditioning to alleviate the more challenging 3D BBox denoising. To the best of our knowledge, REXO is the first diffusion model in the radar perception field conditioned on multi-view radar.
3. **Ground-Level Constraint:** By using prior knowledge that the person is in contact with the ground, the parameters of the 3D BBox are reduced. Based on this, each noise-free 3D BBox preserves geometric constraints in the image plane to be transformed.

We demonstrate the effectiveness of our contributions through evaluations on two open radar datasets.

2 Related Work

Radar-based Object Detection: Learning-based methods have advanced radar detection over traditional model-based approaches (Kay 1998), benefiting from open large-scale radar point cloud datasets like nuScenes (Caesar et al. 2020), Oxford RobotCar (Barnes et al. 2020), and RADIALE (Sheeny et al. 2021). Image-based and point/voxel-based backbones (He et al. 2016; Shi, Li, and Ma 2022) extract semantic features from radar detection points, generate region proposals, and localize objects. High-resolution heatmaps (e.g., K-Radar (Paek et al. 2022), HIBER (Wu et al. 2023), MMVR (Rahman et al. 2024)) and raw ADC data (Yang et al. 2023a) have also been leveraged by previously mentioned RF-Pose (Zhao et al. 2018a), RFMask (Wu et al. 2023), and RETR (Yataka et al. 2024). CubeLearn (Zhao et al. 2023) replaces Fourier transforms with learnable modules for an end-to-end radar pipeline, while RAMP-CNN (Gao et al. 2021) enhances range-angle feature extraction via Doppler cues. More recently, diffusion models have been explored for radar applications (Zhang et al. 2024; Luan et al. 2024; Chi et al. 2024; Fan et al. 2024; Wu et al. 2024). Most efforts, e.g., Radar-Diffusion (Zhang et al. 2024; Luan et al. 2024) and DiffRadar (Wu et al. 2024),

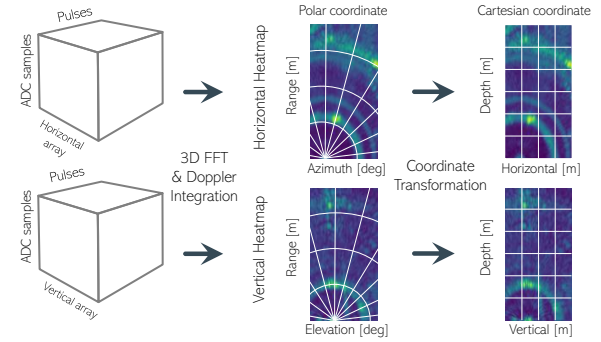


Figure 2: Generation of multi-view heatmaps from raw data.

focus on reconstructing LiDAR-like point clouds from low-resolution radar data, while mmDiff (Fan et al. 2024) estimates and refines pose keypoints from sparse radar points via diffusion process.

Diffusion-based Object Detection: Diffusion models (Song, Meng, and Ermon 2021; Song and Ermon 2019; Rombach et al. 2022; Song et al. 2023) have shown impressive results in tasks such as image and video generation (Ho et al. 2022; Blattmann et al. 2023) and multi-view synthesis (Chen et al. 2023a; Yu et al. 2023). For perception tasks, DiffusionDet (Chen et al. 2023b) first reformulates object detection as a generative denoising process and proposes to model the 2D BBoxes as random parameters in the diffusion process. Diffusion-SS3D (Ho et al. 2023) proposes a diffusion-based detector to enhance the quality of pseudo-labels in semi-supervised 3D object detection by integrating it into a teacher-student framework. CLIFF (Li et al. 2024) further leverages language models to enhance diffusion-based models for open-vocabulary object detection. Diffusion models are also considered for 3D object detection (Xu et al. 2024) in the context of LiDAR-Camera fusion (Xiang, Dräger, and Zhang 2023) and other tasks such as pose estimation (Tan et al. 2024) and semantic segmentation (Gu, Chen, and Xu 2024; Amit et al. 2022).

3 Preliminary

Multi-View Radar Heatmaps derive from raw data captured by horizontal and vertical radar arrays, where sampling reflected pulses across each array builds a 3D data cube of ADC samples, pulse samples and array elements (Fig. 2). A 3D FFT transforms each cube into radar spectra along range, Doppler, and angle (azimuth or elevation). Integrating over Doppler yields 2D polar heatmaps (range–azimuth and range–elevation), which are then mapped to Cartesian coordinates. The resulting heatmaps for frame m are denoted $\mathbf{Y}_{\text{hor}}(m) \in \mathcal{R}^{W \times D}$ and $\mathbf{Y}_{\text{ver}}(m) \in \mathcal{R}^{H \times D}$. Stacking M consecutive frames gives $\mathbf{Y}_{\text{hor}} \in \mathcal{R}^{M \times W \times D}$ and $\mathbf{Y}_{\text{ver}} \in \mathcal{R}^{M \times H \times D}$ for temporal modeling.

Diffusion Models such as the denoising diffusion probabilistic model (DDPM) (Ho, Jain, and Abbeel 2020) and the denoising diffusion implicit model (DDIM) (Song, Meng, and Ermon 2021), define Markovian or non-Markovian forward processes by gradually adding noise to samples \mathbf{x}_0 ,

e.g., image pixels,

$$q(\mathbf{x}_t | \mathbf{x}_0) = \mathcal{N}(\mathbf{x}_t; \sqrt{\bar{\alpha}_t} \mathbf{x}_0, (1 - \bar{\alpha}_t) \mathbf{I}), \quad (1)$$

where $t \in \{0, \dots, T\}$ and $\bar{\alpha}_t = \prod_{s=0}^t (1 - \beta_s)$ with β_s denoting the noise variance schedule. At time t , $\mathbf{x}_t = \sqrt{\bar{\alpha}_t} \mathbf{x}_0 + \sqrt{(1 - \bar{\alpha}_t)} \epsilon$ with $\epsilon \sim \mathcal{N}(\mathbf{0}, \mathbf{I})$.

During training, a noise prediction network is trained to estimate ϵ from \mathbf{x}_t and time index t by minimizing $\min_{\theta} \|\epsilon_{\theta}(\mathbf{x}_t, t) - \epsilon\|^2$, where θ represents the trainable weights. During inference, a random \mathbf{x}_T is drawn from the standard Gaussian distribution and iteratively denoised using the trained $\epsilon_{\theta}(\mathbf{x}_t, t)$ in reverse time: $\mathbf{x}_T \rightarrow \dots \rightarrow \mathbf{x}_t \rightarrow \mathbf{x}_{t-1} \rightarrow \dots \rightarrow \mathbf{x}_0$. Sampling strategies such as DDPM (Ho, Jain, and Abbeel 2020)

$$\mathbf{x}_{t-1} = \left(\mathbf{x}_t - \frac{1 - \alpha_t}{\sqrt{1 - \bar{\alpha}_t}} \epsilon_{\theta}(\mathbf{x}_t, t) \right) / \sqrt{\alpha_t} + \sigma_t \epsilon_t, \quad (2)$$

with $\epsilon_t \sim \mathcal{N}(\mathbf{0}, \mathbf{I})$, and DDIM (Song, Meng, and Ermon 2021) can be used to trade off between quality and speed. More details are in Appendix A.

4 REXO: BBox Diffusion in 3D Radar Space

DiffusionDet (Chen et al. 2023b) reformulates object detection as a denoising diffusion process, treating \mathbf{x}_t as 2D BBox parameters instead of image pixels. As shown in Fig. 3, we extend this to multi-view radar by lifting \mathbf{x}_t to 3D BBoxes in radar coordinates: $\mathbf{x}_t = \{c_x^t, c_y^t, c_z^t, w^t, h^t, d^t\}^\top \in \mathbb{R}^6$, where (c_x^t, c_y^t, c_z^t) defines the center and (w^t, h^t, d^t) the size at time t in the Cartesian {horizontal, vertical, depth} space. Conditioned on radar heatmaps $\{\mathbf{Y}_{\text{hor}}, \mathbf{Y}_{\text{ver}}\}$, REXO performs 3D BBox diffusion in two phases (Fig. 3): 1) a **forward process** that adds noise to ground-truth (GT) BBoxes \mathbf{x}_0 to produce random \mathbf{x}_T during training, and 2) a **reverse process** that denoises random \mathbf{x}_T to estimate noise-free $\hat{\mathbf{x}}_0$ during inference. The denoised BBoxes are also projected to the 2D image plane for supervision in both radar and image domains. We describe REXO in four parts: training, inference, ground-level constraint and loss.

4.1 Training

We describe REXO training, as illustrated in Fig. 4.

Backbone: Taking the two radar heatmaps \mathbf{Y}_{hor} and \mathbf{Y}_{ver} as inputs, a backbone network (e.g., ResNet (He et al. 2016)) generates horizontal-view and vertical-view radar feature maps separately: $\mathbf{Z}_{\text{hor}} = \text{backbone}(\mathbf{Y}_{\text{hor}})$ and $\mathbf{Z}_{\text{ver}} = \text{backbone}(\mathbf{Y}_{\text{ver}})$, where learnable parameters in the backbone are shared across both views. Each feature map is generated as L multi-scale feature maps in $\mathbb{R}^{C \times \frac{W}{s^l} \times \frac{D}{s^l}}$ or $\mathbb{R}^{C \times \frac{H}{s^l} \times \frac{D}{s^l}}$ by using feature pyramid network (Lin et al. 2017) where C, s and $l \in \{1, \dots, L\}$ represent the number of channels, downsampling ratio over the spatial dimension and the pyramid level, respectively.

Initialization of \mathbf{x}_0 and Forward Process to \mathbf{x}_t : For a given number of BBoxes N_{train} to be detected, \mathbf{x}_0 is simply initialized by the 3D BBox GT in the radar space

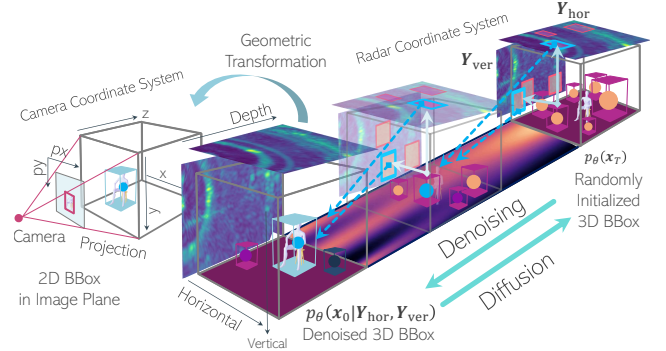


Figure 3: REXO: 1) 3D BBox diffusion process in the radar space; 2) Geometric transformation and 3D-to-2D projection onto the image plane for geometry-aware supervision.

$\mathbf{x}_{\text{radar}} = \{c_x, c_y, c_z, w, h, d\}^\top \in \mathbb{R}^6$ and padded with random 3D BBoxes $\mathbf{x}_{\text{rand}} \sim \mathcal{N}(\mathbf{0}, \mathbf{I}_6)$ if $N_{\text{train}} > N_{\text{GT}}$. The diffused 3D BBox \mathbf{x}_t at time t can be generated as

$$\mathbf{x}_t = \sqrt{\bar{\alpha}_t} \mathbf{x}_0 + \sqrt{1 - \bar{\alpha}_t} \epsilon, \quad (3)$$

where $\epsilon \sim \mathcal{N}(\mathbf{0}, \mathbf{I}_6)$ and $\bar{\alpha}_t$ is defined in Section 3.

Cross-View Radar-Conditioned BBox Detector
DenoisingDet $_{\theta}$ includes explicit cross-view feature association and radar-conditioned 3D BBox detector.

1) **Explicit cross-view feature association:** Given the noisy 3D BBox \mathbf{x}_t in (3), the \mathbf{x}_t -guided cross-view feature association first projects \mathbf{x}_t onto the two radar views, resulting in two 2D BBoxes (purple solid lines of Fig. 1 (d)),

$$\mathbf{x}_{t,\text{hor}} = \{c_x^t, c_z^t, w^t, d^t\}^\top, \mathbf{x}_{t,\text{ver}} = \{c_y^t, c_z^t, h^t, d^t\}^\top, \quad (4)$$

and then crops out the cross-view 2D radar features

$$\begin{aligned} \mathbf{Z}_{\text{hor}}^{\text{crop}} &= \text{RoIAlign}(\mathbf{Z}_{\text{hor}}, \mathbf{x}_{t,\text{hor}}) \in \mathbb{R}^{C \times r \times r}, \\ \mathbf{Z}_{\text{ver}}^{\text{crop}} &= \text{RoIAlign}(\mathbf{Z}_{\text{ver}}, \mathbf{x}_{t,\text{ver}}) \in \mathbb{R}^{C \times r \times r}, \end{aligned} \quad (5)$$

via a standard ROIAlign operation (He et al. 2017), where r denotes a fixed spatial resolution, e.g., $r = 7$. At time t , this process yields N_{train} pairs of associated radar features

$$\mathbf{Z}_{\text{radar}}^{\text{crop}} = \{\mathbf{Z}_{\text{hor}}^{\text{crop}}, \mathbf{Z}_{\text{ver}}^{\text{crop}}\} \in \mathbb{R}^{C \times r \times 2r}, \quad (6)$$

each corresponding to a noisy 3D BBox \mathbf{x}_t .

2) **Radar-conditioned 3D BBox detector:** Conditioned on $\mathbf{Z}_{\text{radar}}^{\text{crop}}$, a BBox detector with learnable weights θ is trained to estimate the BBox $\hat{\mathbf{x}}_0$ and the class scores $\hat{\mathbf{p}}$ as

$$\{\hat{\mathbf{x}}_0, \hat{\mathbf{p}}\} = \text{BBoxDet}_{\theta}(\mathbf{Z}_{\text{radar}}^{\text{crop}}, t), \quad (7)$$

where t specifies the timestep embedding. In our indoor setting, we use a two-class softmax over $\{\text{person}, \text{background}\}$. The class-head can extend to C classes (including background) by using a C -way softmax with cross-entropy.

Grouping all the steps from (4) to (7) results in the DenoisingDet $_{\theta}$ module of Fig. 4:

$$\{\hat{\mathbf{x}}_0, \hat{\mathbf{p}}\} = \text{DenoisingDet}_{\theta}(\mathbf{x}_t, t, \mathbf{Z}_{\text{hor}}, \mathbf{Z}_{\text{ver}}), \quad (8)$$

where all trainable weights θ are inherited from the BBox detector BBoxDet $_{\theta}$. Further details are in Appendix B.

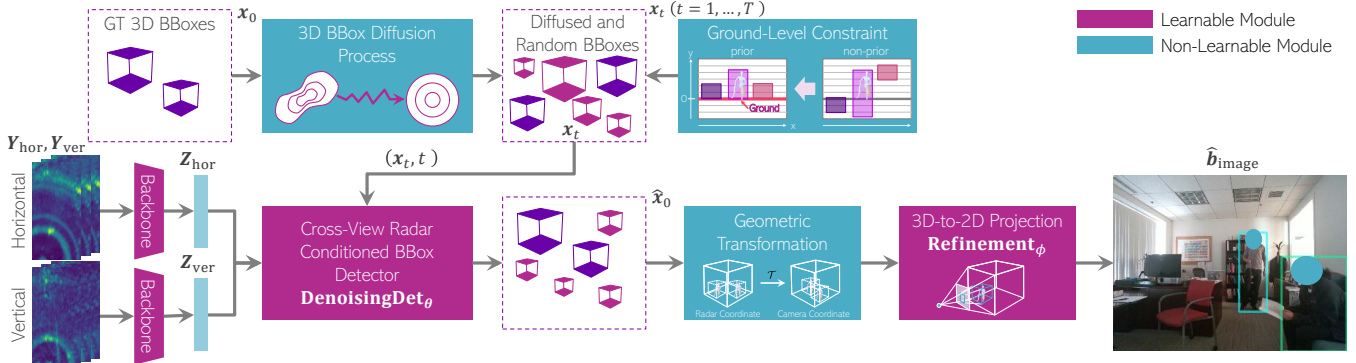


Figure 4: **REXO training:** 1) A shared backbone extracts horizontal/vertical radar features $\{Z_{\text{hor}}, Z_{\text{ver}}\}$; 2) Ground-truth 3D BBoxes x_0 are diffused to noisy x_t ; 3) x_t is grounded using a ground-level constraint; 4) DenoisingDet $_{\theta}$ projects x_t onto both views and uses the aligned features to recover \hat{x}_0 ; 5) A radar-to-camera transform and 3D-to-2D projection yield image BBoxes \hat{b}_{image} , enabling geometry-aware supervision in radar space and image plane.

3D-to-2D Projection with Learnable Refinement.

REXO further projects \hat{x}_0 in (8) into the 2D image plane through the 3D camera coordinate system via a calibrated geometric transformation \mathcal{T} . By setting $\hat{x}_{\text{radar}} = \hat{x}_0$, we convert each of the 8 corners of the corresponding 3D BBox \hat{x}_{radar} using

$$x_{\text{camera}}^i = \mathbf{R}\hat{x}_{\text{radar}}^i + \mathbf{v}, \quad i = 1, 2, \dots, 8, \quad (9)$$

where \hat{x}_{radar}^i is the i -th corner of \hat{x}_{radar} , \mathbf{R} is the calibrated 3D rotation matrix, and \mathbf{v} is the calibrated translation vector. Each 3D corner x_{camera}^i is projected to the image plane through the calibrated pinhole model, and the extrema of the eight projected points yield the initial box \mathbf{b}_{init}

$$\mathbf{b}_{\text{init}} = \{\bar{c}_x, \bar{c}_y, \bar{w}, \bar{h}\}^{\top} = \text{proj}_{\text{init}}(\mathbf{x}_{\text{camera}}). \quad (10)$$

Since \mathbf{b}_{init} systematically overshoots the ground-truth extent (see Appendix C), we attach a refinement module with learnable parameter ϕ to obtain the offset:

$$\Delta \mathbf{b} = \{\Delta \bar{x}, \Delta \bar{y}, \Delta \bar{w}, \Delta \bar{h}\}^{\top} = \text{Refinement}_{\phi}(\mathbf{f}), \quad (11)$$

where $\mathbf{f} = \text{Predictor}(\mathbf{e}_t, Z_{\text{radar}}^{\text{crop}})$ is the time-dependent feature. \mathbf{e}_t denotes the timestep embedding (Ho, Jain, and Abbeel 2020) and Predictor denotes the time-dependent predictor (Chen et al. 2023b) with the radar feature and the embedding (see Appendix B for more details). Applying these offsets produces the final image-plane box \hat{b}_{image} , achieving tighter alignment without sacrificing geometric consistency.

$$\hat{b}_{\text{image}} = \{\bar{c}_x + \bar{w}\Delta \bar{x}, \bar{c}_y + \bar{h}\Delta \bar{y}, e^{\Delta \bar{w}}\bar{w}, e^{\Delta \bar{h}}\bar{h}\}^{\top}. \quad (12)$$

4.2 Inference

REXO infers objects by reversing the diffusion process. Given a target count N , we sample random 3D boxes $x_T \sim \mathcal{N}(\mathbf{0}, \mathbf{I}_6)$ in the radar coordinate system at $t = T$ and denoise them down to $t = 1$.

Denoising Process in 3D Radar Space: With x_t and radar features $\{Z_{\text{hor}}, Z_{\text{ver}}\}$, the trained DenoisingDet $_{\theta}$ in (8) predicts \hat{x}_0 , giving

$$p_{\theta}(x_{t-1} | x_t, Z_{\text{hor}}, Z_{\text{ver}}) = \mathcal{N}(\sqrt{\alpha_{t-1}}x_0 + \gamma\epsilon_{\theta}^{(t)}, \sigma_t^2 \mathbf{I}_6),$$

$$x_{t-1} = \sqrt{\alpha_{t-1}}\hat{x}_0 + \sqrt{1 - \alpha_{t-1} - \sigma_t^2} \cdot \epsilon_{\theta}^{(t)} + \sigma_t \epsilon_t, \quad (13)$$

where $\epsilon_{\theta}^{(t)} = (x_t - \sqrt{\alpha_t}\hat{x}_0)/\sqrt{1 - \alpha_t}$ specifies the direction pointing to the noisy BBox x_t at time t , and $\epsilon_t \sim \mathcal{N}(\mathbf{0}, \mathbf{I}_6)$ represents a random BBox. Note that the denoising step is inherently conditioned on the cross-view radar feature maps via the estimated \hat{x}_0 from the DenoisingDet $_{\theta}$ module.

2D Image Plane BBox Prediction: After the final step, x_0 ($= \hat{x}_{\text{radar}}$) is converted to image plane boxes \hat{b}_{image} via the radar-to-camera transform in (9) and the 3D-to-2D projection of (12). Boxes whose class scores exceed a threshold are output as detections.

4.3 Ground-Level Constraint

Since the BBoxes are now explicitly defined in the 3D radar coordinate system, it is natural to incorporate prior knowledge as a constraint into the diffusion process. Unlike DiffusionDet and RETR, we enforce the reduced five 3D parameters by grounding with $h^t/2$, allowing 3D and 2D gradients to flow jointly and guiding the denoising process under strict geometric constraints. This ensures that objects are correctly positioned on the floor, reflecting realistic spatial relationships (see the Ground-Level Constraint in Fig. 4):

$$x_t = \{c_x^t, h^t/2, c_z^t, w^t, h^t, d^t\}^{\top}. \quad (14)$$

Using this constrained x_t as in (3), REXO predicts N_{train} 3D BBoxes \hat{x}_{radar} and 2D BBoxes \hat{b}_{image} , while preserving geometric consistency.

4.4 Loss Function

To ensure consistency between the radar and image plane representations, we adopt a simplified scheme of the Triplane loss (Yataka et al. 2024) that directly calculates the loss of 3D BBox. REXO employs the Hungarian match cost (Kuhn 1955) with a geometry-aware loss function $\mathcal{L}_{\text{box}}^{\text{GA}}$ computed in both the 3D and 2D spaces:

$$\mathcal{L}_{\text{box}}^{\text{GA}} = \lambda_{3D}\mathcal{L}_{\text{box}}^{\text{3D}}(\mathbf{x}_{\text{radar}}, \hat{x}_{\text{radar}}) + \lambda_{2D}\mathcal{L}_{\text{box}}^{\text{2D}}(\mathbf{b}_{\text{image}}, \hat{b}_{\text{image}}), \quad (15)$$

Table 1: Evaluation on 4 data splits of the MMVR. The gray hatch represents the best performance for each metric.

Method	P1S1			P1S2			P2S1			P2S2		
	AP	AP ₅₀	AP ₇₅									
RFMask	25.53	67.30	15.86	24.46	66.82	11.22	31.37	61.50	27.48	6.03	22.77	0.88
RFMask3D	34.84	69.57	31.74	30.75	76.48	16.23	39.89	80.38	35.35	12.26	37.01	4.34
DETR	35.64	77.59	28.00	28.51	75.90	13.42	29.53	63.08	25.35	9.29	34.69	2.49
RETR	39.62	80.55	33.84	30.16	78.95	15.17	46.75	83.80	46.06	12.45	41.30	4.96
REXO	39.23	73.46	37.83	36.48	87.02	20.51	48.35	85.89	48.38	23.47	64.41	10.44

where the 3D/2D BBox loss is defined as $\mathcal{L}_{\text{box}}^*(\mathbf{x}, \hat{\mathbf{x}}) = \lambda_{\text{GIOU}} \mathcal{L}_{\text{GIOU}}(\mathbf{x}, \hat{\mathbf{x}}) + \lambda_{\text{L}_1} \mathcal{L}_{\text{L}_1}(\mathbf{x}, \hat{\mathbf{x}})$ representing a weighted combination of the generalized intersection over union (GIOU) loss $\mathcal{L}_{\text{GIOU}}$ (Rezatofighi et al. 2019) and the ℓ_1 loss \mathcal{L}_{L_1} , and the coefficients λ balance the relative contribution of each loss term. REXO determines the optimal assignment σ_{GA}^* by minimizing the matching cost that combines the original classification cost $\mathcal{L}_{\text{class}}$ and $\mathcal{L}_{\text{box}}^{\text{GA}}$.

5 Experiments

We demonstrate the effectiveness of REXO through evaluations on two open radar datasets: HIBER (Wu et al. 2023) and MMVR (Rahman et al. 2024).

5.1 Setup

High-Resolution Indoor Radar Datasets: MMVR includes multi-view radar heatmaps collected from over 25 human subjects across 6 rooms over a span of 9 days. It consists of 345K data frames collected in 2 protocols: 1) Protocol 1 (P1: Open Foreground) with 107.9K frames in an open-foreground room with a single subject; and 2) Protocol 2 (P2: Cluttered Space) with 237.9K frames in 5 cluttered rooms with single and multiple subjects. Under each protocol, two data splits are defined to evaluate radar perception performance: 1) S1: a random data split and 2) S2: a cross-session, unseen split.

HIBER, partially released, includes multi-view radar heatmaps from 10 human subjects in a single room but from different angles with multiple data splits. In our evaluation, we used the “WALK” data split, consisting of 73.5K data frames with one subject walking in the room. For both datasets, annotations such as 3D BBoxes in the radar coordinate system and 2D image plane BBoxes are provided to train the baseline methods and REXO.

Implementation: We consider RFMask (Wu et al. 2023), DETR (Carion et al. 2020) and RETR (Yataka et al. 2024) as baseline methods. Additionally, we evaluate a 3D extension of RFMask, referred to as RFMask3D (see Appendix D for details), that takes the two radar views as inputs for BBox prediction. Since RFMask and DETR originally compute the BBox loss only in the 2D horizontal radar plane and the 2D image plane, respectively, we follow the implementation of RETR and enhance both methods with a unified bi-plane BBox loss. Furthermore, we introduce a DETR variant with a top- K feature selection, allowing it to take features from both horizontal and vertical heatmaps as input. For RETR, we set the number of object queries to 10. To ensure a fair comparison, we also set $N_{\text{train}} = 10$ for REXO during

Table 2: Evaluation on the WALK data split of the HIBER.

Method	WALK		
	AP	AP ₅₀	AP ₇₅
RFMask	17.77	52.46	6.78
RFMask3D	16.58	48.10	6.53
DETR	14.45	47.33	4.25
RETR	22.09	59.83	10.99
REXO	25.33	62.55	15.83

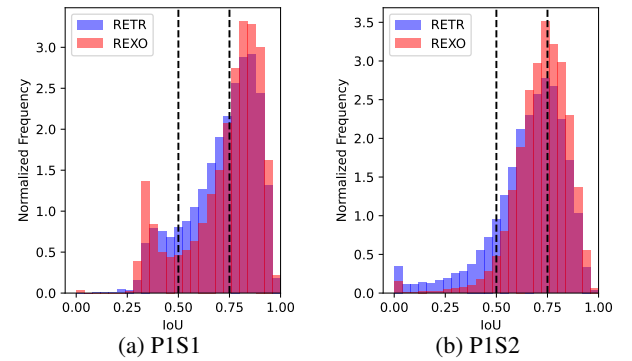


Figure 5: AP breakdowns with IoU histograms on MMVR. training. All methods are evaluated using $M = 4$ consecutive radar frames. Additional hyperparameter settings are provided in Appendix E.

Metrics: We evaluate performance using average precision (AP) at two IoU thresholds of 0.5 (AP₅₀) and 0.75 (AP₇₅), along with the mean AP (AP) computed over thresholds in the range of [0.5 : 0.05 : 0.95]. For detailed metric definitions, refer to Appendix F.

5.2 Main Results

MMVR: Table 1 presents the results under the four combinations of two protocols and two data splits of the MMVR dataset. REXO demonstrates significant performance improvements in P1S2, P2S1, and P2S2. Notably, in P2S2 where the test radar frames contain an entirely unseen environment during training, REXO outperforms the best baseline RETR by a large margin, boosting AP from 12.45 to 23.47, highlighting its strong generalization capabilities. Surprisingly, under the simplest combination P1S1 where a single subject is recorded in the same room with a random data split, REXO’s performance is slightly lower than that of RETR, particularly on the metric AP₅₀.

To understand these differences, we break down the AP into IoU histograms for (a) P1S1 and (b) P1S2, as illustrated in Fig. 5, where blue and red histograms represent the IoU

λ_{3D}	λ_{2D}	AP	Method	N_{train}	AP	N	REXO	RETR	Steps	AP	Method	AP
0.00	1.00	0.98	RETR	10	12.45	2	8.87	8.36	1	23.48	DiffusionDet	20.75
0.50	1.00	4.23		20	9.85	10	23.48	12.45	3	24.01	REXO (Horizontal)	22.75
1.00	0.10	15.55		50	8.49	20	23.00	6.57	5	24.12	REXO (Vertical)	7.18
1.00	0.50	19.38	REXO	10	23.47	40	22.32	3.63	7	24.17	REXO (Both Views)	23.47
1.00	1.00	23.47		20	20.94	60	21.94	2.65	9	24.25		
				50	19.67	80	21.70	2.16	10	24.27		

(a) Strong 2D (λ_{2D})/3D (λ_{3D}) supervision improves performance.

(b) # of BBoxes for training. REXO remains stable.

(c) # of BBoxes for inference. REXO sustains its AP as N increases.

(e) DiffusionDet vs. single-/multi-view REXO. Multi-view achieves the best AP.

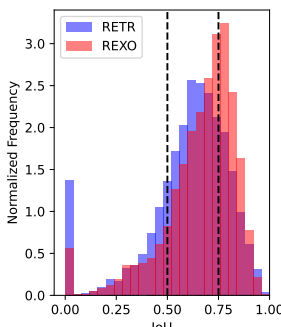
Table 5: Ablation study under P2S2 on MMVR.

Grounding	AP (P2S2)	AP (WALK)
\times	22.67	21.11
\checkmark	23.47	25.33

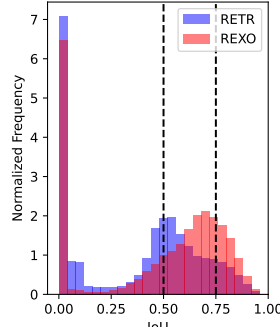
Table 3: The ground-level constraint can improve the detection performance on both datasets.

D [cm]	AP
$D \leq 20$	9.93
$D > 20$	23.47

Table 4: AP drops when depth difference D is less than 20 cm.



(a) Seen Frames: REXO exhibits a similar histogram to that observed in P1S2.



(b) Unseen Frames: REXO has more high-quality predictions than RETR.

Figure 6: AP breakdowns with IoU histograms on MMVR.

distributions for RETR and REXO, respectively, and the left and right dotted lines mark the two IoU thresholds at 0.5 and 0.75. It is seen that in Fig. 5a, the excess of RETR over REXO (blue areas) over the IoU interval [0.5, 0.75] is greater than that of REXO over RETR (pink areas) over the interval [0.75, 1.0], explaining RETR’s higher AP_{50} under P1S1. Meanwhile, REXO has better AP_{75} as it provides more high-quality predictions with IoU above 0.75.

HIBER: Table 2 presents the results evaluated on the “WALK” data split of the HIBER dataset. For baselines, RFMask, RFMask3D, and DETR show comparable performance, while RETR exhibits the strongest baseline performance. REXO outperforms RETR across all evaluation metrics with an AP of 25.33, surpassing RETR’s AP at 22.09. REXO attains AP_{50} of 62.55 and AP_{75} of 15.83, demonstrating strong performance in both low- and high-IoU BBox performance evaluations. This ability to consistently outperform the baselines across different IoU thresholds indicates REXO’s robustness in capturing object localization with relatively better accuracy.

5.3 Ablation Study

We present ablation studies for REXO under the most challenging “P2S2” of the MMVR dataset. Full results are provided in Appendix G.

Effectiveness of Ground-Level Constraint: Table 3 reports the effect of ground-level constraint. In MMVR, the subject stands on the ground or sits in a chair, so the constraint is effective. The table shows that we also evaluated the HIBER dataset as a supplement and observed a significant improvement in performance. It should be noted that constraint is not always accurate when the subject jumps or stands on an obstacle, but it is still effective in terms of stabilizing inference.

2D vs. 3D Supervision Strength: Table 5a compares the various weight parameters λ_{3D} and λ_{2D} in (15). The results highlight the necessity of accounting for the loss of both the 3D BBox and the 2D BBox, and the importance of the prediction accuracy of the 3D BBox, especially in the radar coordinate system, for the prediction accuracy of the 2D BBox on the image plane. The image plane supervision is essential to train the learnable refinement module. Strong 2D (image plane) and 3D (radar space) supervision yields better performance.

Number of BBoxes in Training: We evaluate the impact of N_{train} , the number of BBoxes for REXO and the number of queries for RETR, on the three AP metrics in Table 5b. It is seen that AP tends to decrease as N_{train} increases for both methods, but this may be due to the number of BBoxes being too large relative to the number of subjects, since the maximum number of subjects in the MMVR dataset is three per frame.

Dynamic Number of BBoxes in Inference: Table 5c evaluates the impact of varying the number of BBoxes during inference. While RETR exhibits a sharp performance decline when the number of queries exceeds 10, REXO experiences a much smaller decrease. This robustness in handling varying numbers of BBoxes during inference is a direct advantage inherited from DiffusionDet.

Number of Iteration Steps: Table 5d presents REXO’s performance as the number of iteration steps increases. Increasing the steps from 1 to 10 yields improvements of +0.78 in AP, showing consistent gains with more iterations. We also report runtime and FPS on a single NVIDIA RTX

	Input		Output Predicted 2D BBox in Image Plane			RGB (not input and output) (Dark Blue BBox is GT in image plane)	
	Hor	Ver	Output denoised 3D BBox in Radar Coord. with REXO	RFMask	RETR		
d8s2/006							
d8s4/008							
d8s5/008							
d8s6/008							

Figure 7: Visualization of unseen frames in P2S2 of MMVR: The left column shows the radar heatmaps, followed by the second column displaying predicted/GT 3D BBoxes in the radar space. Corresponding image-plane 2D BBox predictions are shown in the middle column for two baselines (RFMask and RETR) and REXO, with purple segmentation masks overlaid to illustrate the alignment with human GT. The right column presents the RGB images with GT 2D BBoxes for qualitative check.

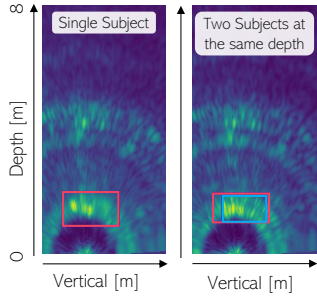


Figure 8: Vertical radar heatmaps when a single subject (left) and two subjects (right) are at the same depth.

6000: 60 ms (17 FPS) for 1 step, 255 ms (4 FPS) for 5 steps, and 483 ms (2 FPS) for 10 steps. While more steps improve accuracy, they incur higher latency. Thus, using 5 steps offers a practical trade-off between detection performance and runtime efficiency for indoor human sensing.

Additional comparison with DiffusionDet and REXO: Table 5e confirms that our REXO (both views) outperforms the original DiffusionDet with radar heatmaps, which denotes our REXO is more appropriate for our radar settings. It also suggests the horizontal view (i.e., bird's-eye view) is more critical than the vertical view for detection since the vertical view cannot separate the azimuth position.

5.4 Challenging Cases

To better understand challenging configurations, we provide additional analysis for two scenarios: 1) when two subjects are at a similar depth; and 2) generalization over unseen environments. For 1), Fig. 8 compares vertical heatmaps when a single subject (left) and two subjects (right) present at nearly the same depth but at different heights. When multiple subjects are at the same depth, the reflections from different subjects overlap and form more complex patterns than that for a single subject, potentially leading to failed cross-view feature association and radar-conditioned denoising steps. As confirmed in Table 4, AP drops significantly when the depth difference D is less than 20 cm based on the evaluation over P2S2 of MMVR. For 2), we divide the test radar frames in P2S2 of MMVR into “Seen” and “Unseen” frames, and analyze their APs using IoU histograms in Fig. 6. For the “Seen” frames, REXO exhibits a histogram similar to one observed in P1S2. In contrast, for the “Unseen” frames, REXO clearly dominates the IoU range of $[0.75, 1]$, while RETR shows a heavier concentration around an IoU of 0.5.

Fig. 7 further visualizes selected “Unseen” frames from a room never encountered during training in P2S2. It is seen that 2D BBox predictions by REXO align more closely with human segmentation masks (purple pixels) than those of RETR and RFMask. This improvement is potentially due to the explicit cross-view feature association, which strengthens consistency across radar views even in new environ-

ments, yielding better generalization. More visualization examples are provided in Appendix G.

6 Conclusion

For indoor radar perception, we proposed REXO, a novel multi-view radar object detection method that refines 3D BBoxes through a diffusion process. By explicitly guiding cross-view radar feature association and incorporating ground-level constraint, REXO achieves consistent performance improvements on two open indoor radar datasets over a list of strong baselines.

References

Adib, F.; Hsu, C.-Y.; Mao, H.; Katabi, D.; and Durand, F. 2015. RF-Capture: Capturing a Coarse Human Figure Through a Wall. In *SIGGRAPH Asia*.

Amit, T.; Shaharbany, T.; Nachmani, E.; and Wolf, L. 2022. SegDiff: Image Segmentation with Diffusion Probabilistic Models. arXiv:2112.00390.

Barnes, D.; Gadd, M.; Murcatt, P.; Newman, P.; and Posner, I. 2020. The Oxford radar robotcar dataset: A radar extension to the Oxford robotcar dataset. In *International Conference on Robotics and Automation*, 6433–6438.

Blattmann, A.; Rombach, R.; Ling, H.; Dockhorn, T.; Kim, S. W.; Fidler, S.; and Kreis, K. 2023. Align Your Latents: High-Resolution Video Synthesis With Latent Diffusion Models. In *Proceedings of the IEEE/CVF Conference on Computer Vision and Pattern Recognition (CVPR)*, 22563–22575.

Caesar, H.; Bankiti, V.; Lang, A. H.; Vora, S.; Lioung, V. E.; Xu, Q.; Krishnan, A.; Pan, Y.; Baldan, G.; and Beijbom, O. 2020. nuScenes: A multimodal dataset for autonomous driving. In *Proceedings of the IEEE/CVF Conference on Computer Vision and Pattern Recognition*, 11621–11631.

Carion, N.; Massa, F.; Synnaeve, G.; Usunier, N.; Kirillov, A.; and Zagoruyko, S. 2020. End-to-End Object Detection with Transformers. In *European Conference on Computer Vision (ECCV)*, 213–229.

Chen, H.; Gu, J.; Chen, A.; Tian, W.; Tu, Z.; Liu, L.; and Su, H. 2023a. Single-Stage Diffusion NeRF: A Unified Approach to 3D Generation and Reconstruction. In *Proceedings of the IEEE/CVF International Conference on Computer Vision (ICCV)*, 2416–2425.

Chen, S.; Sun, P.; Song, Y.; and Luo, P. 2023b. DiffusionDet: Diffusion Model for Object Detection. In *IEEE/CVF International Conference on Computer Vision (ICCV)*, 19773–19786.

Chi, G.; Yang, Z.; Wu, C.; Xu, J.; Gao, Y.; Liu, Y.; and Han, T. X. 2024. RF-Diffusion: Radio Signal Generation via Time-Frequency Diffusion. arXiv:2404.09140.

Everingham, M.; Van Gool, L.; Williams, C. K. I.; Winn, J.; and Zisserman, A. 2010. The PASCAL Visual Object Classes (VOC) Challenge. *International Journal of Computer Vision*, 88(2): 303–338.

Fan, J.; Yang, J.; Xu, Y.; and Xie, L. 2024. Diffusion Model Is a Good Pose Estimator from 3D RF-Vision. In *European Conference on Computer Vision (ECCV)*, 1–18. Cham.

Gao, X.; Xing, G.; Roy, S.; and Liu, H. 2021. RAMP-CNN: A Novel Neural Network for Enhanced Automotive Radar Object Recognition. *IEEE Sensors Journal*, 21(4): 5119–5132.

Gu, Z.; Chen, H.; and Xu, Z. 2024. DiffusionInst: Diffusion Model for Instance Segmentation. In *IEEE International Conference on Acoustics, Speech and Signal Processing (ICASSP)*, 2730–2734.

He, K.; Gkioxari, G.; Dollár, P.; and Girshick, R. 2017. Mask R-CNN. In *IEEE International Conference on Computer Vision (ICCV)*, 2980–2988.

He, K.; Zhang, X.; Ren, S.; and Sun, J. 2016. Deep Residual Learning for Image Recognition. In *IEEE/CVF Conference on Computer Vision and Pattern Recognition (CVPR)*, 770–778.

Ho, C.-J.; Tai, C.-H.; Lin, Y.-Y.; Yang, M.-H.; and Tsai, Y.-H. 2023. Diffusion-SS3D: Diffusion Model for Semi-supervised 3D Object Detection. In *Advances in Neural Information Processing Systems (NeurIPS)*, volume 36, 49100–49112.

Ho, J.; Jain, A.; and Abbeel, P. 2020. Denoising Diffusion Probabilistic Models. In *Advances in Neural Information Processing Systems (NeurIPS)*, volume 33, 6840–6851.

Ho, J.; Salimans, T.; Gritsenko, A.; Chan, W.; Norouzi, M.; and Fleet, D. J. 2022. Video Diffusion Models. In *Advances in Neural Information Processing Systems (NeurIPS)*, volume 35, 8633–8646.

Hosang, J.; Benenson, R.; Dollár, P.; and Schiele, B. 2016. What Makes for Effective Detection Proposals? *IEEE Transactions on Pattern Analysis and Machine Intelligence*, 38(4): 814–830.

Kay, S. M. 1998. *Fundamentals of Statistical Signal Processing: Detection Theory*. Prentice Hall.

Kuhn, H. W. 1955. The Hungarian method for the assignment problem. *Naval research logistics quarterly*, 2(1-2): 83–97.

Lee, S.-P.; Kini, N. P.; Peng, W.-H.; Ma, C.-W.; and Hwang, J.-N. 2023. HuPR: A Benchmark for Human Pose Estimation Using Millimeter Wave Radar. In *IEEE/CVF Winter Conference on Applications of Computer Vision (WACV)*, 5715–5724.

Li, W.; Liu, X.; Ma, J.; and Yuan, Y. 2024. CLIFF: Continual Latent Diffusion for Open-Vocabulary Object Detection. In *European Conference on Computer Vision (ECCV)*.

Lin, T.-Y.; Dollár, P.; Girshick, R.; He, K.; Hariharan, B.; and Belongie, S. 2017. Feature Pyramid Networks for Object Detection. In *IEEE Conference on Computer Vision and Pattern Recognition (CVPR)*, 936–944.

Lu, C. X.; Rosa, S.; Zhao, P.; Wang, B.; Chen, C.; Stankovic, J. A.; Trigoni, N.; and Markham, A. 2020. See through smoke: robust indoor mapping with low-cost mmWave radar. In *The 18th International Conference on Mobile Systems, Applications, and Services (MobiSys)*, 14–27.

Luan, K.; Shi, C.; Wang, N.; Cheng, Y.; Lu, H.; and Chen, X. 2024. Diffusion-Based Point Cloud Super-Resolution for mmWave Radar Data. In *IEEE International Conference on Robotics and Automation (ICRA)*, 11171–11177.

Paek, D.-H.; et al. 2022. K-Radar: 4D Radar Object Detection for Autonomous Driving in Various Weather Conditions. In *NeurIPS*, volume 35, 3819–3829.

Pandharipande, A.; Cheng, C.-H.; Dauwels, J.; Gurbuz, S. Z.; Ibanez-Guzman, J.; Li, G.; Piazzoni, A.; Wang, P.; and Santra, A. 2023. Sensing and Machine Learning for Automotive Perception: A Review. *IEEE Sensors Journal*, 23(11): 11097–11115.

Rahman, M. M.; Yataka, R.; Kato, S.; Wang, P.; Li, P.; Cardace, A.; and Boufounos, P. 2024. MMVR: Millimeter-wave Multi-View Radar Dataset and Benchmark for Indoor Perception. In *European Conference on Computer Vision (ECCV)*, 306–322. ISBN 978-3-031-72986-7.

Ren, S.; He, K.; Girshick, R.; and Sun, J. 2017. Faster R-CNN: Towards Real-Time Object Detection with Region Proposal Networks. *IEEE Transactions on Pattern Analysis and Machine Intelligence*, 39(6): 1137–1149.

Rezatofighi, H.; Tsai, N.; Gwak, J.; Sadeghian, A.; Reid, I.; and Savarese, S. 2019. Generalized Intersection Over Union: A Metric and a Loss for Bounding Box Regression. In *IEEE/CVF Conference on Computer Vision and Pattern Recognition (CVPR)*, 658–666.

Rombach, R.; Blattmann, A.; Lorenz, D.; Esser, P.; and Ommer, B. 2022. High-Resolution Image Synthesis With Latent Diffusion Models. In *Proceedings of the IEEE/CVF Conference on Computer Vision and Pattern Recognition (CVPR)*, 10684–10695.

Sengupta, A.; Jin, F.; Zhang, R.; and Cao, S. 2020. mmPose: Real-Time Human Skeletal Posture Estimation Using mmWave Radars and CNNs. *IEEE Sensors Journal*, 20(17): 10032–10044.

Sheeny, M.; De Pellegrin, E.; Mukherjee, S.; Ahrabian, A.; Wang, S.; and Wallace, A. 2021. RADIATE: A Radar Dataset for Automotive Perception in Bad Weather. In *IEEE International Conference on Robotics and Automation (ICRA)*, 1–7.

Shi, G.; Li, R.; and Ma, C. 2022. PillarNet: Real-Time and High-Performance Pillar-Based 3D Object Detection. In *European Conference on Computer Vision (ECCV)*, 35–52.

Skog, M.; Kotlyar, O.; Kubelka, V.; and Magnusson, M. 2024. Human Detection from 4D Radar Data in Low-Visibility Field Conditions. *arXiv:2404.05307*.

Song, J.; Meng, C.; and Ermon, S. 2021. Denoising Diffusion Implicit Models. In *International Conference on Learning Representations (ICLR)*.

Song, Y.; Dhariwal, P.; Chen, M.; and Sutskever, I. 2023. Consistency Models. In *Proceedings of the 40th International Conference on Machine Learning*, volume 202 of *Proceedings of Machine Learning Research*, 32211–32252.

Song, Y.; and Ermon, S. 2019. Generative Modeling by Estimating Gradients of the Data Distribution. In *Advances in Neural Information Processing Systems (NeurIPS)*, volume 32.

Sun, S.; Petropulu, A. P.; and Poor, H. V. 2020. MIMO Radar for Advanced Driver-Assistance Systems and Autonomous Driving: Advantages and Challenges. *IEEE Signal Processing Magazine*, 37(4): 98–117.

Tan, D.; Chen, H.; Tian, W.; and Xiong, L. 2024. DiffusionRegPose: Enhancing Multi-Person Pose Estimation Using a Diffusion-Based End-to-End Regression Approach. In *IEEE/CVF Conference on Computer Vision and Pattern Recognition (CVPR)*, 2230–2239.

Wu, J.; Geng, R.; Li, Y.; Zhang, D.; Lu, Z.; Hu, Y.; and Chen, Y. 2024. Diffradar: High-Quality mmWave Radar Perception With Diffusion Probabilistic Model. In *IEEE International Conference on Acoustics, Speech and Signal Processing (ICASSP)*, 8291–8295.

Wu, Z.; Zhang, D.; Xie, C.; Yu, C.; Chen, J.; Hu, Y.; and Chen, Y. 2023. RFMask: A Simple Baseline for Human Silhouette Segmentation With Radio Signals. *IEEE Transactions on Multimedia*, 25: 4730–4741.

Xiang, X.; Dräger, S.; and Zhang, J. 2023. 3Diffusion-Det: Diffusion Model for 3D Object Detection with Robust LiDAR-Camera Fusion. *ArXiv*, abs/2311.03742.

Xu, C.; Ling, H.; Fidler, S.; and Litany, O. 2024. 3DiffTec-tion: 3D Object Detection with Geometry-Aware Diffusion Features. In *IEEE/CVF Conference on Computer Vision and Pattern Recognition (CVPR)*, 10617–10627.

Yang, B.; Khatri, I.; Happold, M.; and Chen, C. 2023a. ADCNet: Learning from Raw Radar Data via Distillation. *arXiv:2303.11420*.

Yang, J.; Huang, H.; Zhou, Y.; Chen, X.; Xu, Y.; Yuan, S.; Zou, H.; Lu, C. X.; and Xie, L. 2023b. MM-Fi: Multi-Modal Non-Intrusive 4D Human Dataset for Versatile Wireless Sensing. In *Advances in Neural Information Processing Systems (NeurIPS)*, volume 36, 18756–18768.

Yao, S.; Guan, R.; Peng, Z.; Xu, C.; Shi, Y.; Ding, W.; Lim, E. G.; Yue, Y.; Seo, H.; Man, K. L.; Ma, J.; Zhu, X.; and Yue, Y. 2024. Exploring Radar Data Representations in Autonomous Driving: A Comprehensive Review. *arXiv:2312.04861*.

Yataka, R.; Cardace, A.; Wang, P.; Boufounos, P.; and Takahashi, R. 2024. RETR: Multi-View Radar Detection Transformer for Indoor Perception. In *Advances in Neural Information Processing Systems (NeurIPS)*, volume 37, 19839–19869.

Yu, J. J.; Forghani, F.; Derpanis, K. G.; and Brubaker, M. A. 2023. Long-Term Photometric Consistent Novel View Synthesis with Diffusion Models. In *Proceedings of the IEEE/CVF International Conference on Computer Vision (ICCV)*, 7094–7104.

Zhang, R.; Xue, D.; Wang, Y.; Geng, R.; and Gao, F. 2024. Towards Dense and Accurate Radar Perception via Efficient Cross-Modal Diffusion Model. *IEEE Robotics and Automation Letters*, 9(9): 7429–7436.

Zhao, M.; Li, T.; Alsheikh, M. A.; Tian, Y.; Zhao, H.; Torralba, A.; and Katabi, D. 2018a. Through-Wall Human Pose Estimation Using Radio Signals. In *IEEE/CVF Conference on Computer Vision and Pattern Recognition (CVPR)*, 7356–7365.

Zhao, M.; Tian, Y.; Zhao, H.; Alsheikh, M. A.; Li, T.; Hristov, R.; Kabelac, Z.; Katabi, D.; and Torralba, A. 2018b.

RF-based 3D skeletons. In *The Conference of the ACM Special Interest Group on Data Communication (SIGCOMM)*, 267–281.

Zhao, M.; Yue, S.; Katabi, D.; Jaakkola, T. S.; and Bianchi, M. T. 2017. Learning Sleep Stages from Radio Signals: A Conditional Adversarial Architecture. In *International Conference on Machine Learning (ICML)*, volume 70, 4100–4109.

Zhao, P.; Lu, C. X.; Wang, B.; Trigoni, N.; and Markham, A. 2023. CubeLearn: End-to-End Learning for Human Motion Recognition From Raw mmWave Radar Signals. *IEEE Internet of Things Journal*, 10(12): 10236–10249.

A Details on Diffusion Models

Denoising Diffusion Probabilistic Models (DDPM) (Ho, Jain, and Abbeel 2020) and Denoising Diffusion Implicit Models (DDIM) (Song, Meng, and Ermon 2021) are latent variable models designed to approximate the data distribution $q(\mathbf{x}_0)$ using a generative model distribution $p_\theta(\mathbf{x}_0)$. The generative model structure is expressed as:

$$p_\theta(\mathbf{x}_0) = \int p_\theta(\mathbf{x}_{0:T}) d\mathbf{x}_{1:T}, \quad (16)$$

$$p_\theta(\mathbf{x}_{0:T}) = p_\theta(\mathbf{x}_T) \prod_{t=1}^T p_\theta^{(t)}(\mathbf{x}_{t-1} | \mathbf{x}_t), \quad (17)$$

where $\mathbf{x}_{1:T}$ are latent variables defined in the same space as \mathbf{x}_0 . The generative process reverses the forward diffusion process, transforming noise \mathbf{x}_T into \mathbf{x}_0 over T steps. Both models share a training objective based on maximizing the variational lower bound (ELBO):

$$\begin{aligned} & \max_{\theta} \mathbb{E}_{q(\mathbf{x}_0)} [\log p_\theta(\mathbf{x}_0)] \\ & \leq \max_{\theta} \mathbb{E}_{q(\mathbf{x}_{0:T})} [\log p_\theta(\mathbf{x}_{0:T}) - \log q(\mathbf{x}_{1:T} | \mathbf{x}_0)]. \end{aligned} \quad (18)$$

In both cases, the forward process $q(\mathbf{x}_{1:T} | \mathbf{x}_0)$ has no learnable parameter, simplifying training to focus on the generative process.

DDPM (Ho, Jain, and Abbeel 2020): The forward process progressively adds Gaussian noise to \mathbf{x}_0 through a Markov chain:

$$q(\mathbf{x}_t | \mathbf{x}_{t-1}) = \mathcal{N} \left(\sqrt{\frac{\alpha_t}{\alpha_{t-1}}} \mathbf{x}_{t-1}, \left(1 - \frac{\alpha_t}{\alpha_{t-1}} \right) \mathbf{I} \right), \quad (19)$$

where α_t is a decreasing sequence. This transforms \mathbf{x}_0 into nearly pure Gaussian noise \mathbf{x}_T , leading to a direct sampling of the \mathbf{x}_t from \mathbf{x}_0 :

$$q(\mathbf{x}_t | \mathbf{x}_0) = \mathcal{N} (\mathbf{x}_t; \sqrt{\bar{\alpha}_t} \mathbf{x}_0, (1 - \bar{\alpha}_t) \mathbf{I}), \quad (20)$$

where $\bar{\alpha}_t := \prod_{s=0}^t \alpha_s = \prod_{s=0}^t (1 - \beta_s)$ with β_s denoting the noise variance schedule. The reverse process approximates this process backward:

$$p_\theta^{(t)}(\mathbf{x}_{t-1} | \mathbf{x}_t) = \mathcal{N} \left(\mu_\theta^{(t)}(\mathbf{x}_t), \sigma_t^2 \mathbf{I} \right), \quad (21)$$

where $\mu_\theta^{(t)}(\mathbf{x}_t) = \frac{1}{\sqrt{\bar{\alpha}_t}} \left(\mathbf{x}_t - \frac{\beta_t}{\sqrt{1 - \bar{\alpha}_t}} \epsilon_\theta^{(t)}(\mathbf{x}_t) \right)$ is a learnable function and $\epsilon_\theta^{(t)}$ is designed with a neural network model with learnable parameter θ . The sampling can be done following (2). The loss function is designed to minimize the discrepancy in predicting noise:

$$L_\gamma(\epsilon_\theta) = \sum_{t=1}^T \gamma_t \mathbb{E}_{\mathbf{x}_0, \epsilon} \left[\|\epsilon_\theta^{(t)}(\mathbf{x}_t) - \epsilon\|_2^2 \right], \quad (22)$$

where $\epsilon \sim \mathcal{N}(\mathbf{0}, \mathbf{I})$ is Gaussian noise, and γ_t are weights.

DDIM (Song, Meng, and Ermon 2021): DDIM generalizes the forward process to a non-Markovian framework which can be derived from Bayes' rule:

$$q(\mathbf{x}_t | \mathbf{x}_{t-1}, \mathbf{x}_0) = \frac{q(\mathbf{x}_{t-1} | \mathbf{x}_t, \mathbf{x}_0) q(\mathbf{x}_t | \mathbf{x}_0)}{q(\mathbf{x}_{t-1} | \mathbf{x}_0)}, \quad (23)$$

where $q(\mathbf{x}_t | \mathbf{x}_0)$ and $q(\mathbf{x}_{t-1} | \mathbf{x}_0)$ are defined with (20) and

$$\begin{aligned} & q(\mathbf{x}_{t-1} | \mathbf{x}_t, \mathbf{x}_0) \\ & = \mathcal{N} \left(\sqrt{\alpha_{t-1}} \mathbf{x}_0 + \sqrt{1 - \alpha_{t-1} - \sigma_t^2} \epsilon^{(t)}, \sigma_t^2 \mathbf{I} \right), \end{aligned} \quad (24)$$

with

$$\epsilon^{(t)} = \frac{\mathbf{x}_t - \sqrt{\alpha_t} \mathbf{x}_0}{\sqrt{1 - \alpha_t}}. \quad (25)$$

Different from DDPM, this process maintains a direct dependence on the original data \mathbf{x}_0 at each step. The reverse process in DDIM reconstructs \mathbf{x}_0 as

$$\mathbf{x}_{t-1} = \sqrt{\alpha_{t-1}} \hat{\mathbf{x}}_0 + \sqrt{1 - \alpha_{t-1} - \sigma_t^2} \cdot \epsilon^t + \sigma_t \epsilon_t, \quad (26)$$

$$\epsilon^{(t)} = \frac{\mathbf{x}_t - \sqrt{\alpha_t} \hat{\mathbf{x}}_0}{\sqrt{1 - \alpha_t}}, \quad (27)$$

where $\epsilon^{(t)}$ is the estimated noise from \mathbf{x}_0 to \mathbf{x}_t . The loss function remains identical to that in DDPM which uses the neural network $\epsilon_\theta^{(t)}(\mathbf{x}_t)$, ensuring the compatibility in training.

DDIM enables a faster sampling by reducing the number of steps T in the sampling process. A subset of latent variables $\{\mathbf{x}_{\tau_1}, \dots, \mathbf{x}_{\tau_S}\}$ is defined where τ is an increasing sub-sequence of $[1, \dots, T]$ of length S , and sampling occurs over this shortened trajectory:

$$\begin{aligned} \mathbf{x}_{\tau_{i-1}} & = \sqrt{\alpha_{\tau_{i-1}}} \hat{\mathbf{x}}_0 + \sqrt{1 - \alpha_{\tau_{i-1}} - \sigma_{\tau_i}^2} \cdot \epsilon^{(\tau_i)} + \sigma_{\tau_i} \epsilon_{\tau_i}, \\ \epsilon^{(\tau_i)} & = \frac{\mathbf{x}_{\tau_i} - \sqrt{\alpha_{\tau_i}} \hat{\mathbf{x}}_0}{\sqrt{1 - \alpha_{\tau_i}}}. \end{aligned} \quad (28)$$

For instance, when $S \ll T$, computational efficiency is significantly improved. This method allows a pre-trained DDPM model to be reused while achieving $10 \times$ to $50 \times$ faster sampling. This acceleration is particularly beneficial for scenarios requiring low-latency processing such as perception tasks.

For REXO training in Fig. 4 and inference, we construct a DenoisingDet $_\theta$ that directly predicts \mathbf{x}_0 , similar to the above DDIM and DiffusionDet (Chen et al. 2023b). This direct estimation of \mathbf{x}_0 allows us to compute the set-prediction loss in DETR (Carion et al. 2020) over both radar and camera coordinate systems. As a result, the noise prediction network $\epsilon^{(\tau_i)}$ is a function of the predicted $\hat{\mathbf{x}}_0$.

B Details of Cross-View Radar-Conditioned Denoising Detector

Fig. 9 illustrates the overall architecture of the proposed cross-view radar-conditioned denoising detector

$$\hat{\mathbf{x}}_0 = \text{DenoisingDet}_\theta(\mathbf{x}_t, t, \mathbf{Z}_{\text{hor}}, \mathbf{Z}_{\text{ver}}), \quad (29)$$

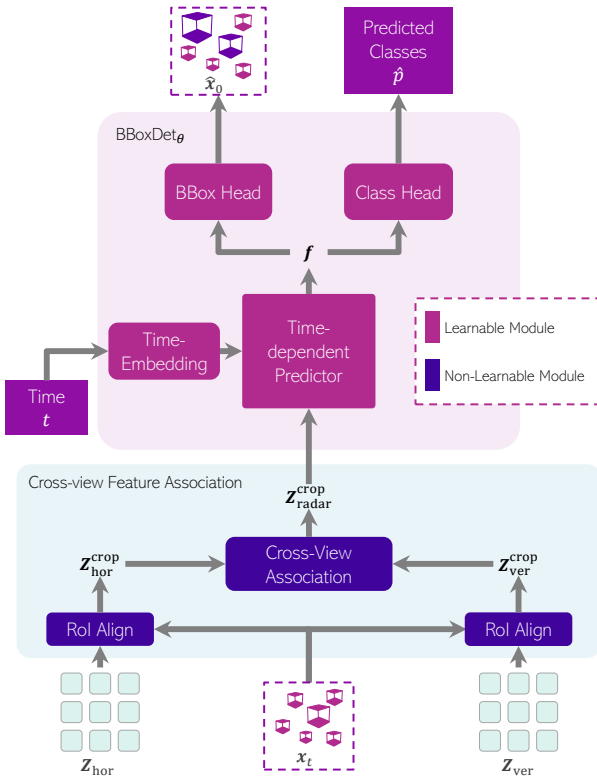


Figure 9: Overall architecture of the cross-view radar-conditioned denoising detector $\text{DenoisingDet}_\theta$.

which takes as input the noisy 3D BBox set \mathbf{x}_t , the time index t , and the two radar view backbone features $\{Z_{\text{hor}}, Z_{\text{ver}}\}$. The output is a direct estimation of \mathbf{x}_0 . Specifically, $\text{DenoisingDet}_\theta$ comprises two key modules:

- **1. Cross-view feature association;**
- **2. BBox detector BBoxDet_θ .**

The cross-view feature association module was explained in (4)-(6), which involves the 3D-to-2D BBox projection of (4), feature cropping via the ROIAlign operation of (5), and the feature aggregation of (6), yielding $Z_{\text{radar}}^{\text{crop}} = \{Z_{\text{hor}}^{\text{crop}}, Z_{\text{ver}}^{\text{crop}}\} \in \mathbb{R}^{C \times r \times 2r}$ in Fig. 9 (blue hatch).

The BBox detector module, BBoxDet_θ , first incorporates a time-dependent predictor, Predictor, designed to extract time-dependent features \mathbf{f} from the aligned cross-view radar features $Z_{\text{radar}}^{\text{crop}}$ and the time-embedding of t (Ho, Jain, and Abbeel 2020),

$$\mathbf{f} = \text{Predictor}(\mathbf{e}_t, Z_{\text{radar}}^{\text{crop}}), \quad (30)$$

where $\mathbf{e}_t = \text{Embedding}(t)$ is a time-embedding of time t . In the Predictor, self-attention is applied to the cross-view radar features $Z_{\text{radar}}^{\text{crop}}$ to reason about the relations between objects. Then, the features are enhanced by applying the dynamic convolution to each 3D ROI feature. Finally, they are fed into the diffusion process by time-embedding to obtain the feature \mathbf{f} .

Using the time-dependent feature \mathbf{f} , the BBox and Class heads are used to predict the BBoxes $\hat{\mathbf{x}}_0$ and the class labels.

In the BBox head, the offset $\Delta\mathbf{x}$ is first computed as

$$\begin{aligned} \Delta\mathbf{x} &= \{\Delta x, \Delta y, \Delta z, \Delta w, \Delta h, \Delta d\}^\top \in \mathbb{R}^6 \\ &= \text{FFN}_{\text{offset}}^{\text{3D}}(\mathbf{f}), \end{aligned} \quad (31)$$

where $\text{FFN}_{\text{offset}}^{\text{3D}} : \mathbb{R}^D \rightarrow \mathbb{R}^6$ represents a feed-forward network (FFN) to estimate the 3D BBox offsets and each $\Delta*$ denotes the offset for the corresponding BBox parameter (x, y, z, w, h, d). To ensure numerical stability, the values of $\Delta w, \Delta h$ and Δd are clipped to a maximum of $\log(10^5/16)$. The BBox estimate $\hat{\mathbf{x}}_0$ is then computed using a linear update for the BBox center position and an exponential scaling over the axis length offsets $\{e^{\Delta w}, e^{\Delta h}, e^{\Delta d}\}$:

$$\hat{\mathbf{x}}_0 = \{c_x + w\Delta x, c_y + h\Delta y, c_z + d\Delta z, e^{\Delta w}w, e^{\Delta h}h, e^{\Delta d}d\}^\top. \quad (32)$$

In the class head, the class scores can be predicted as \hat{p} . The classification loss evaluates the alignment between the predicted objects and GT classes, serving as a crucial component in object detection tasks. The classification loss is defined as:

$$\mathcal{L}_{\text{class}} = - \sum_{i=1}^{N_{\text{train}}} \log \hat{p}_{\hat{\sigma}(i)}(c_i), \quad (33)$$

where c_i is the GT class label, $\hat{p}_{\hat{\sigma}(i)}(c_i)$ denotes the predicted probability for class c_i , and $\hat{\sigma}(i)$ represents the optimal matching computed by the Hungarian algorithm. It is a permutation that defines the one-to-one correspondence between the GT object set and the predicted set. Additionally, when the GT class is \emptyset (no object), the loss term is down-weighted to address class imbalance. This design improves the model's performance in predicting positive examples (objects present in the image).

C Details of 3D-to-2D Projection and Necessity of the Refinement Module

We present the detailed explanations for 3D-to-2D projection and necessity of the refinement module. Given a 3D BBox which consists of its eight vertices

$$\{\mathbf{x}_{\text{camera}}^i \in \mathbb{R}^3 \mid i = 1, \dots, 8\}, \quad (34)$$

where each $\mathbf{x}_{\text{camera}}^i$ is expressed in the 3D camera coordinate system, our goal is to compute the corresponding 2D BBox $\mathbf{b}_{\text{init}} \in \mathbb{R}^4$, defined by its center coordinates (x_c, y_c) and its width w and height h . To achieve this, we define a projection function with a pinhole camera model as a concrete expression of (10):

$$\text{proj}_{\text{pinhole}} : \mathbb{R}^3 \rightarrow \mathbb{R}^2 : (X, Y, Z) \mapsto (p_x, p_y). \quad (35)$$

In this model, the projection of the point $\mathbf{x}_{\text{camera}}^* = (X, Y, Z)$ onto the image plane is given by

$$p_x = \frac{f_x X}{Z} + c_x, \quad p_y = \frac{f_y Y}{Z} + c_y, \quad (36)$$

where f_x and f_y are the focal lengths along the x and y axes (in pixels), and (c_x, c_y) represents the coordinates of

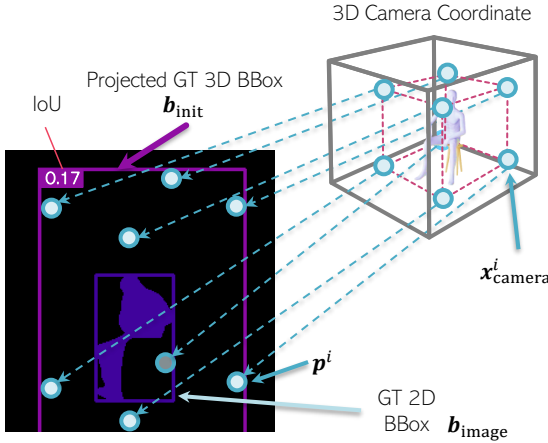


Figure 10: A direct projection of 3D BBoxes to the 2D image plane results in oversized 2D BBoxes. A learnable module is used to refine the projected BBoxes close to the 2D BBox GT.

the principal point in the image. In homogeneous coordinates, this mapping can be expressed as

$$\lambda \begin{pmatrix} p_x \\ p_y \\ 1 \end{pmatrix} = \begin{pmatrix} f_x & 0 & c_x \\ 0 & f_y & c_y \\ 0 & 0 & 1 \end{pmatrix} \begin{pmatrix} X \\ Y \\ Z \end{pmatrix}, \quad (37)$$

with the scaling factor $\lambda = Z$. Thus, for each vertex, the projection onto the image plane is given by:

$$p^i = \text{proj}_{\text{pinhole}}(x_{\text{camera}}^i), \quad \text{for } i = 1, \dots, 8, \quad (38)$$

where $p^i = (p_x^i, p_y^i)$ represents the 2D coordinates of the projected point in the image plane. Once the eight vertices have been projected, the extreme coordinates on the image plane are determined as:

$$u_{\min} = \min_i \{p_x^i\}, \quad u_{\max} = \max_i \{p_x^i\}, \quad (39)$$

$$v_{\min} = \min_i \{p_y^i\}, \quad v_{\max} = \max_i \{p_y^i\}. \quad (40)$$

Using these extremes, the center coordinates, width, and height of the 2D BBox are computed by:

$$x_c = \frac{u_{\min} + u_{\max}}{2}, \quad y_c = \frac{v_{\min} + v_{\max}}{2}, \quad (41)$$

$$w = u_{\max} - u_{\min}, \quad h = v_{\max} - v_{\min}. \quad (42)$$

Thus, the final 2D BBox can be obtained as:

$$b_{\text{init}} = (x_c, y_c, w, h). \quad (43)$$

The 2D BBoxes obtained by projection, as shown by the purple box b_{init} in Fig. 10, are often too large. This occurs because projecting the eight vertices x_{camera}^i captures the depth information from the camera, which causes both the near and far parts of the object to be displayed in a 3D manner. As a result, to accurately predict the 2D BBox b_{image} on the image plane, we must use a refinement module. This module reduces the size of the initial BBox, as illustrated by the blue boxes in Fig. 10.

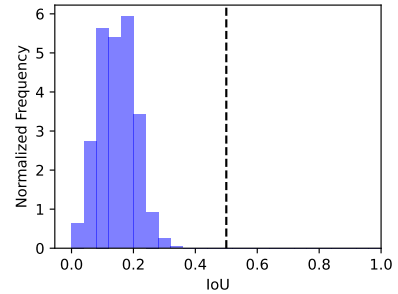


Figure 11: IoU histogram when no image plane supervision. Almost all IoU values are lower than 0.5, resulting in 0 AP.

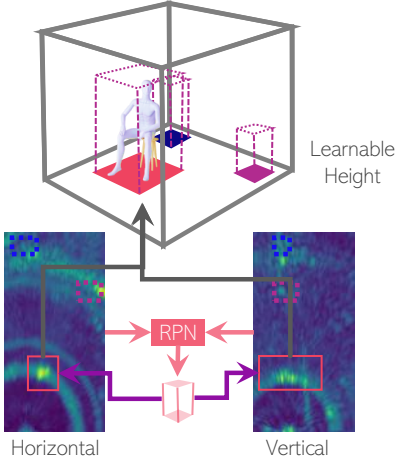


Figure 12: 3D Proposals with RFMask3D.

To better understand the need for refinement, we calculated the Intersection over Union (IoU) between the ground-truth (GT) 3D BBoxes (projected from the 3D space) and the GT 2D BBoxes (defined on the image plane). The histogram of IoU values in Fig. 11 shows a roughly Gaussian distribution with a peak around 0.15, and nearly all IoU values are below 0.5. In fact, in Fig. 10, the IoU is 0.17. This indicates that if we do not apply refinement, even when the 3D BBoxes are correctly predicted in the radar coordinate system, the average precision (AP) on the image plane would be zero. Therefore, our REXO method uses a refinement module.

D RFMask3D as a Baseline

As one of the baselines in our evaluation experiments, we constructed RFMask3D by extending RFMask (Wu et al. 2023) to 3D. RFMask uses a region proposal network (RPN) to extract regions of interest (RoIs) from a horizontal heatmap based on 2D anchor boxes and predicts 3D BBoxes in the 3D radar coordinate system by combining them with fixed heights. By designing an RPN that uses 3D anchor boxes, we explicitly extract 3D RoIs from both horizontal and vertical heatmaps, as shown in Fig. 12, enabling the estimation of 3D BBoxes. Unlike RFMask, this method allows for the learning of height as well.

Table 6: Details of hyper-parameters. Fixed height for the HIBER dataset depends on the environment.

Name		Notation	Value			
			P1S1	P1S2	P2S1	P2S2
Data	# of training	-	86579	70266	190441	118280
	# of validation	-	10538	24398	23899	33841
	# of test	-	10785	13238	23458	85677
	Input radar heatmap size	$H \times W$	256×128	256×128	256×128	256×128
	Segmentation mask size	$H \times W$	240×320	240×320	240×320	240×320
	Resolution of range	cm	11.5	11.5	11.5	11.5
	Resolution of azimuth	deg.	1.3	1.3	1.3	1.3
Model	Resolution of elevation	deg.	1.3	1.3	1.3	1.3
	Scale	-	log	log	log	log
	Backbone	-	ResNet18	ResNet18	ResNet18	ResNet18
	# of input consecutive radar frames	-	4	4	4	4
	Extracted feature map size	$H/s \times W/s$	64×32	64×32	64×32	64×32
	Threshold for detection	-	0.5	0.5	0.5	0.5
	Loss weight for GIoU on radar coordinate system	λ_{GIoU}	2.0	2.0	2.0	2.0
Training	Loss weight for GIoU on image plane	λ_{GIoU}	2.0	2.0	2.0	2.0
	Loss weight for L_1 on radar coordinate system	λ_{L_1}	5.0	5.0	5.0	5.0
	Loss weight for L_1 on image plane	λ_{L_1}	5.0	5.0	5.0	5.0
	Loss weight for radar	λ_{3D}	1.0	1.0	1.0	1.0
	Loss weight for image	λ_{2D}	1.0	1.0	1.0	1.0
	Batch size	-	32	32	32	32
	Epoch for detection	-	100	100	100	100
Training	Patience for early stopping	-	5	5	5	5
	Check val every n epoch for early stopping	-	2	2	2	2
	Optimizer	-	AdamW	AdamW	AdamW	AdamW
	Learning rate	-	1e-4	1e-4	1e-4	1e-4
	Sheduler	-	Cosine	Cosine	Cosine	Cosine
	Maximum number of epochs for sheduler	-	100	100	100	100
	Weight decay	-	1e-3	1e-3	1e-3	1e-3
Training	# of workers	-	8	8	8	8
	GPU (NVIDIA)	-	A40	A40	A40	A40
	# of GPUs	-	1	1	1	1
	Approximate training time	day	1	1	2	2

Table 7: Full Result of Table 1 under P1S1 on MMVR dataset.

Method	AP	AP ₅₀	AP ₇₅	AR ₁	AR ₁₀
RFMask	25.53	67.30	15.86	38.90	38.91
RFMask3D	34.84	69.57	31.74	44.88	44.88
DETR	35.64	77.59	28.00	-	-
RETR	39.62	80.55	33.84	51.90	53.42
REXO	39.23	73.46	37.83	48.58	48.58

Table 8: Full Result of Table 1 under P1S2 on MMVR dataset.

Method	AP	AP ₅₀	AP ₇₅	AR ₁	AR ₁₀
RFMask	24.46	66.82	11.22	34.07	34.53
RFMask3D	30.75	76.48	16.23	40.28	40.29
DETR	28.51	75.90	13.42	-	-
RETR	30.16	78.95	15.17	42.93	42.93
REXO	36.48	87.02	20.51	47.70	47.71

E Hyperparameters for Performance Evaluation

The hyper-parameters used in our experiments of Section 5 are shown in Table 6. The table is divided into three parts, Data, Model, and Training, each with parameter names, notations, and values for each dataset.

F Definition of Metrics

Mean Intersection over Union: We adopt average precision on intersection over union (IoU) (Everingham et al. 2010) as an evaluation metric. IoU is the ratio of the overlap to the union of a predicted BBox A and annotated BBox B as:

$$\text{IoU}(A, B) = \frac{|A \cap B|}{|A \cup B|}. \quad (44)$$

Table 9: Full Result of Table 1 under P2S1 on MMVR dataset.

Method	AP	AP ₅₀	AP ₇₅	AR ₁	AR ₁₀
RFMask	31.37	61.50	27.48	33.07	38.21
RFMask3D	39.89	80.38	35.35	36.81	48.54
DETR	29.53	63.08	25.35	-	-
RETR	46.75	83.80	46.06	42.19	57.39
REXO	48.35	85.89	48.38	43.52	57.88

Table 10: Full Result of Table 1 under P2S2 on MMVR dataset.

Method	AP	AP ₅₀	AP ₇₅	AR ₁	AR ₁₀
RFMask	6.03	22.77	0.88	9.25	12.09
RFMask3D	12.26	37.01	4.34	18.91	19.52
DETR	9.29	34.69	2.49	20.68	22.82
RETR	12.45	41.30	4.96	19.96	21.58
REXO	23.47	64.41	10.44	30.65	33.44

Average Precision: Average Precision (AP) can then be defined as the area under the interpolated precision-recall curve, which can be calculated using the following formula:

$$AP = \sum_{i=1}^{n-1} (r_{i+1} - r_i) p_{\text{interp}}(r_{i+1}), \quad (45)$$

$$p_{\text{interp}}(r) = \max_{r' \geq r} p(r'), \quad (46)$$

where the interpolated precision p_{interp} at a certain recall level r is defined as the highest precision found for any recall level $r' \geq r$. We present three variants of average precision: AP₅₀, AP₇₅, and AP, where the former two represent the loose and strict constraints of IoU, while AP is the averaged score over 10 different IoU thresholds in [0.5, 0.95] with a step size of 0.05.

Average Recall: Average recall (AR) (Hosang et al. 2016) between 0.5 and 1 of IoU overlap threshold can be computed by averaging over the overlaps of each annotation gt_i with the closest matched proposal, that is integrating over the $y : \text{recall}$ axis of the plot instead of the $x : \text{IoU overlap threshold}$ axis. Let o be the IoU overlap and $\text{recall}(o)$ the function. Let $\text{IoU}(gt_i)$ denote the IoU between the annotation gt_i and the closest detection proposal:

$$AR = 2 \int_{0.5}^1 \text{recall}(o) do \quad (47)$$

$$= \frac{2}{n} \sum_{i=1}^n \max(\text{IoU}(gt_i) - 0.5, 0). \quad (48)$$

The following are some variations of AR:

- AR₁: AR given one detection per frame;
- AR₁₀: AR given 10 detection per frame;
- AR₁₀₀: AR given 100 detection per frame.

Table 11: Full Result of Table 2 under WALK on HIBER dataset.

Method	AP	AP ₅₀	AP ₇₅	AR ₁	AR ₁₀
RFMask	17.77	52.46	6.78	32.71	32.71
RFMask3D	16.58	48.10	6.53	29.89	29.89
DETR	14.45	47.33	4.25	28.64	28.64
RETR	22.09	59.83	10.99	35.16	35.16
REXO	25.33	62.55	15.83	20.03	37.54

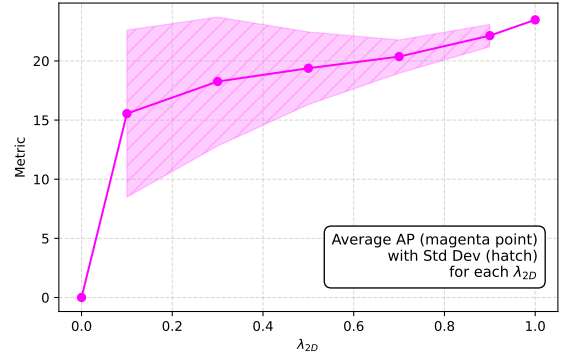


Figure 13: Result of Table 5a: The effect of 2D image supervision with loss weight λ_{2D} while keeping $\lambda_{3D} = 1.0$.

G Ablation Study

Complete Results: Tables 7, 8, 9 and 10 show the complete results of Table 1, including AR. We added the metric regarding average recall explained in Appendix F. The results show that the same trends as in Table 1 also apply to AR. In particular, the generalization performance of Split P2S2 has improved significantly.

2D Image Supervision: Fig. 13 shows the AP results of Table 5a, which compares the various weight parameter λ_{2D} while keeping $\lambda_{3D} = 1.0$ in (15). Each point denotes the mean of three trials, and the hatching denotes the standard deviation. The table shows that it is possible to achieve high performance by using both the loss of the 3D BBox in the radar coordinate system and the loss of the 2D BBox on the image plane. Also, the figure shows that values of $\lambda_{2D} \leq 0.5$ exhibit a larger standard deviation. In other words, there is a general upward trend, reflecting the trade-off between 2D and 3D losses.

Number of BBoxes in Training: Table 12 shows the complete results of Table 5b. From the table, we can see that AP₅₀ drops significantly for RETR as the number of queries increases, but REXO maintains a high level of accuracy. On the other hand, there is no significant fluctuation in AR, and RETR and REXO have similar trends. However, REXO has a significantly higher performance.

Dynamic Number of BBoxes in Inference: Fig. 14 shows the AP50 results of Table 5c. The red line shows the results of REXO, and the blue line shows the results of

Table 12: Full Result of Table 5b: The number of BBoxes in Training.

Method	N_{train}	AP	AP ₅₀	AP ₇₅	AR ₁	AR ₁₀
RETR	10	12.45	41.30	4.96	19.96	21.58
RETR	20	9.85	31.01	4.48	17.90	18.72
RETR	50	8.49	29.76	2.53	17.12	18.91
REXO	10	23.47	64.41	10.44	30.65	33.44
REXO	20	20.94	65.03	5.90	27.45	29.63
REXO	50	19.67	61.44	5.63	26.30	28.45

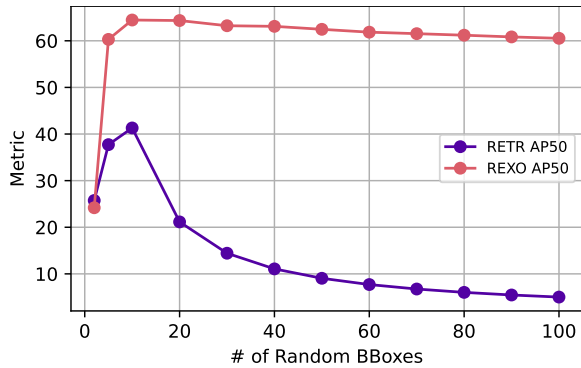


Figure 14: Full Result of Table 5c: Dynamic number of BBoxes in inference.

RETR. When the number of BBoxes used in the inference is increased, we can see that RETR performs much worse, while REXO maintains roughly the same performance for all BBoxes. This is because RETR uses queries that require training, and, combined with the results in Table 12, a significant deviation from the number of objects in the data will lead to a decrease in performance. On the other hand, REXO always uses random initial BBoxes, so it does not require training and can handle a more flexible number of BBoxes regardless of the number of objects.

Number of Iteration Steps: Fig. 15 shows the AP₅₀ results of Table 5d. The number of steps corresponds to S , as explained in Appendix A. From the figure, we can see that REXO’s performance improves as the number of steps S increases.

Impact of Denoising One Parameter: Table 13 evaluated two variants: denoising only c_z (center depth) or d (depth extent) for 10 steps, while fixing the other parameters after 1 step. Both variants maintain strong performance, though jointly denoising all parameters (10 steps) yields the best result.

Ground-Level Constraint: The effectiveness of prior-constrained 3D BBox diffusion is evaluated in terms of convergence during training. The training curve is shown in Fig. 16. The horizontal axis represents the number of training steps and the vertical axis represents AP. From this figure, it can be seen that convergence is faster when prior-constrained 3D BBox diffusion is applied than when it is not.

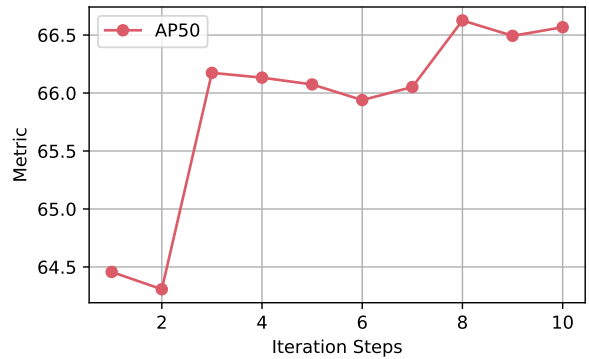


Figure 15: Full Result of Table 5d: # of denoising steps S . More steps slightly improve the detection.

Table 13: Effect of denoising only one parameter.

Denoised Param.	# of steps	AP	AP ₅₀	AP ₇₅
c_z	10	23.39	65.71	10.13
d	10	23.42	65.86	10.12
All	10	24.27	66.57	11.18

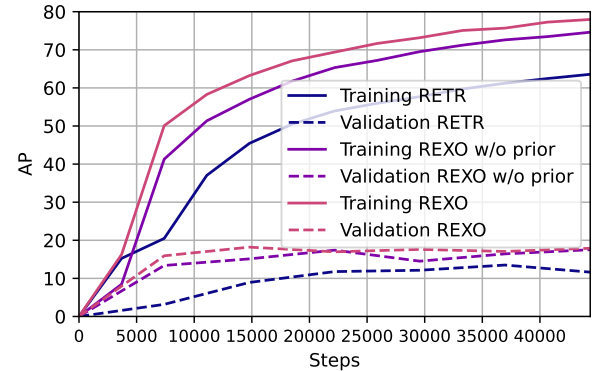


Figure 16: REXO can contribute to fast convergence by using a ground-level constraint for 3D BBox Diffusion.

Performance also remained high on the validation set when prior-constrained 3D BBox diffusion was applied, suggesting that it improves both fast convergence and generalization performance.

Analysis of Failure Cases: We provide failure cases in Fig. 17. These are all results of “Unseen,” which means the environment that is not included in the training data (d8). As with d8s1 and d8s3, REXO may sometimes predict inaccurate positions, although less frequently than RETR and RFMask. In addition, there are cases where false negatives occur, such as with d8s2, d8s4, d8s5, and d8s6. In particular, it is thought to be difficult to capture the characteristics of individuals that are far away from the radar, such as with d8s2, because the resolution becomes coarse. In addition, REXO frequently gets false positives such as d8s2 - d8s6, so adjusting the threshold is important.

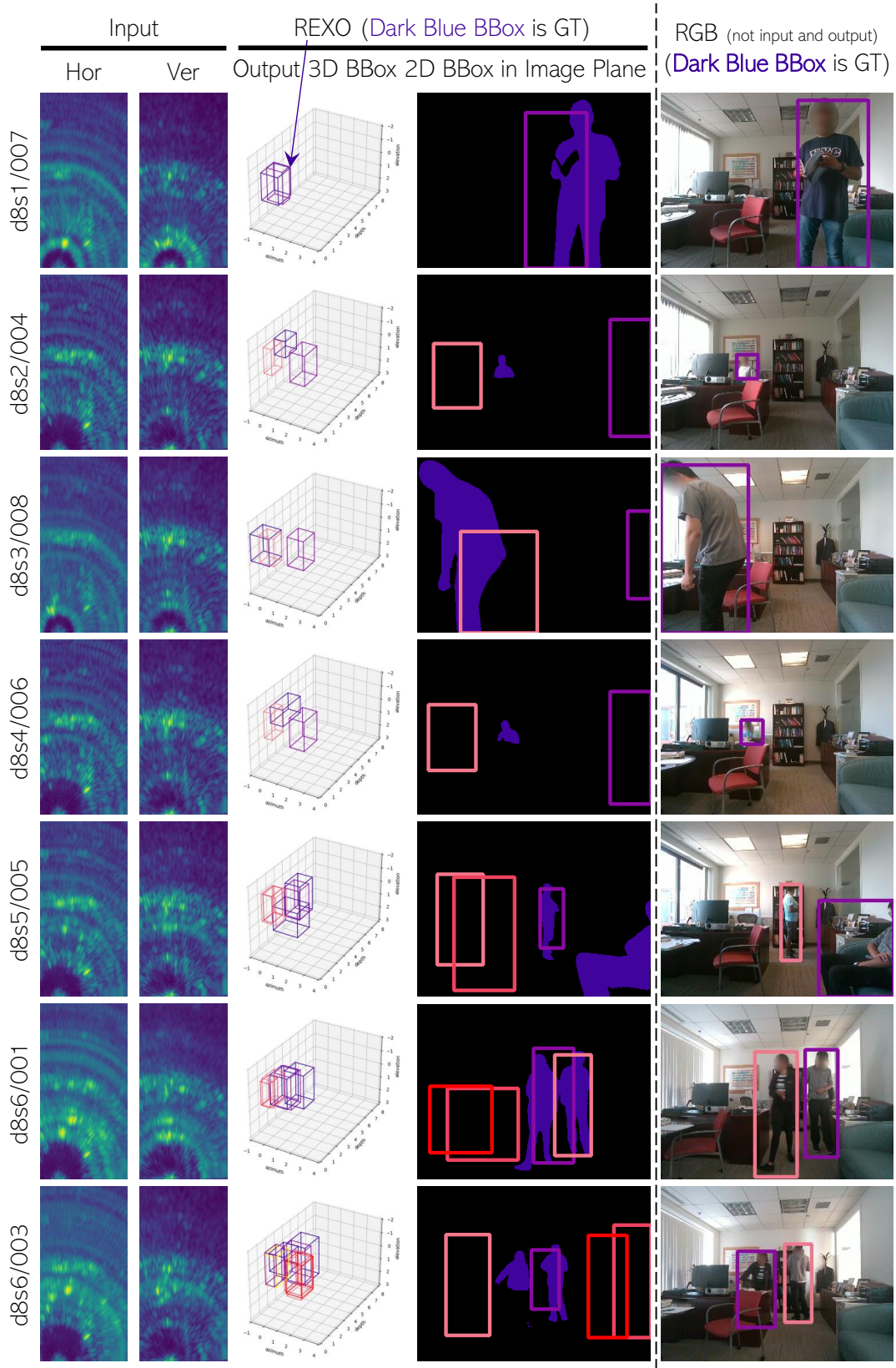


Figure 17: Visualization of failure cases. Each row indicates the segment name used from the P2S2 test dataset.